Supporting Material :

Torsion profiling of proteins using magnetic particles

A. van Reenen,[†]* F. Gutiérrez-Mejía,[†] L. J. van IJzendoorn,[†] and M. W. J. Prins[†‡]

[†]Eindhoven University of Technology, Eindhoven, The Netherlands; and [‡]Philips Research, Eindhoven, The Netherlands

Contents

S1 Model of unbound particle behavior in a rotating field

To study the influence of Brownian rotation on the experimentally determined breakdown frequency, a numerical model of the particle behavior was developed. Based on experimental observations (e.g. see Fig. 2 *b* and Fig. 3 *b*), it is found that above a field strength of approximately 2 mT, the overall ferromagnetic moment of the particles remagnetizes over 180 degrees. Moreover, (see Fig. 4 *a*) remagnetization occurs already at an angular difference between field and magnetic moment of about 35 degrees. As discussed in more detail in Supporting Material S8, the small angle is most likely due to a granular distribution of ferromagnetic moments within one particle, adding up to a net non-zero magnetic moment (μ_{net}) of the particle.

Assuming a distribution of magnetic grains, the magnetic torque τ_m may be expressed as follows:

$$\tau_m = B\sum_{i=1}^{N}\mu_i \sin\left(\theta_i - \theta_{field}\right) \qquad \text{with } \mu_{net} = \sum_{i=1}^{N}\mu_i \sin\left(\theta_i\right) > 0 \tag{S1}$$

with B the field strength, μ_i the size of magnetic moment i, θ_{field} the field orientation and θ_i the orientation of magnetic moment i. We assume a distribution of equally sized magnetic moments over a total angular range which is less than 180°, i.e.

$$\tau_m = \mu B\sum_{i=-N}^{N}\sin\left(i\cdot\Delta\theta - \theta_{field}\right) \qquad \text{with } N\cdot\Delta\theta < 90° \tag{S2}$$

Note that Eq. S2 describes the torque exerted on a distribution of static moments, which do not remagnetize. Remagnetization occurs when the coercive field is overcome, and as a consequence θ_i is history dependent. Numerically, this problem can be treated by evaluating at each next step the previous orientation of the separate magnetic moments with respect to the field orientation. In case the coercive field is overcome, 180° is added to the orientation of the corresponding magnetic moment i.

Using the time step approach to compute the magnetic torque at time t, the angular displacement after a certain time-step Δt is determined following a forward Euler numerical scheme. Specifically, the magnetic torque is balanced with the hydrodynamic drag and inertia is neglected based on the low Reynolds number for this system (Re < 10^{-3} at 10 Hz rotation). From the torque balance, the angular velocity at time t can be computed and is used to determine the particle orientation at $t + \Delta t$, i.e.

$$\theta\left(t+\Delta t\right) = \theta\left(t\right) + \Delta t\cdot\frac{\tau_m + \tau_{BR}}{8\pi\eta C_{drag}R^3} \tag{S3}$$

with η the dynamic viscosity, C_{drag} a correction factor to account for the vicinity of the surface, estimated at 1.22 (14); R the particle radius and Δt the numerical timestep.

Besides the magnetic torque and the hydrodynamic drag, Brownian rotation is included in our model by adding a random torque τ_{BR}. Brownian rotation is numerically implemented based on a

first-order time stepping scheme as proposed by Grassia et al (17). The effective Brownian rotation torque is calculated at each new time-step, i.e.

$$\tau_{BR} = r_n \sqrt{\frac{24 k_B T \cdot 8\pi\eta C_{drag} R^3}{\Delta t}} \tag{S4}$$

with k_B the Boltzmann's constant, T the temperature and r_n is a random number from a normalized Gaussian distribution with mean 0, and consequently a variance of 1/12. The factor 24 in Eq. S4 is a consequence of this variance.

First, the numerical scheme for Brownian rotation was validated by setting the magnetic torque to zero, i.e. via $B = 0$. As a typical timestep, 0.2 ms was taken and the numerical scheme was executed. As shown in Fig. S1, the angular displacement due to Brownian rotation is accurately simulated using Eq. S3 with $\Delta t = 0.2$ ms. The displacement after a single time-step as well as after many time-steps agree with the root-mean-squared values as expected, based on a rotational diffusion constant according to the Stokes-Einstein relation.

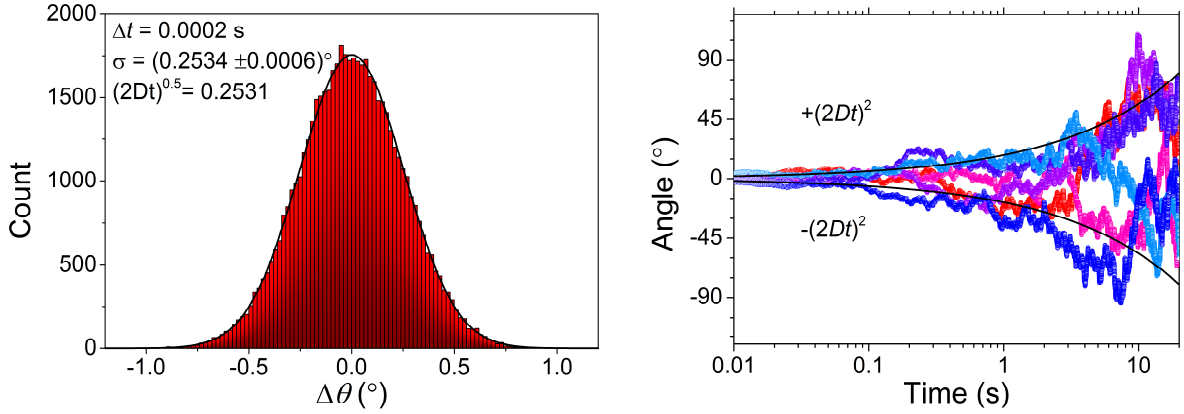

FIGURE S1 (left) Histogram of computed angular displacement due to Brownian motion over 0.2 ms. In total 50.000 computations were made to obtain the distribution. The black curve represents a Gaussian distribution with the width which corresponds to the root-mean-squared angular displacement as analytically expected for Brownian rotation. (right) Simulated angular displacement over time in the absence of a magnetic torque. The simulated time-step is 0.2 ms. The black curves represent the analytically expected rms angular displacement due to Brownian rotation.

Subsequently, the magnetic torque is added corresponding to Eq. S2 in combination with an evaluation at each time-step of the magnetic field with respect to the coercive fields of the separate magnetic moments, allowing remagnetization over 180 degrees, in correspondence to experimental observations. The angular moment distribution is chosen to be close to the experimentally determined magnetic torque and the angle difference upon remagnetization. In particular, 22 magnetic moments ($N = 11$) of equal size $\mu = 1.08$ Am^2 are spread out over 126° with $\Delta\theta = 6°$.

In Fig. S2, the time-dependent behavior is shown for a 5 mT magnetic field rotating at a frequency of 1.4 Hz (left) and 2 Hz (right). Numerical data is shown with and without Brownian rotation included. In particular, for the case of 1.4 Hz with Brownian motion, the computed curve looks closely similar to the experimental curve obtained at this frequency and magnetic field strength, which is shown in Fig. 2 *a*. Based on this qualitative agreement, and also on the observation that the simulated particles also remagnetize at the experimentally observed angular difference around 35 degrees, leads us to conclude that our model can accurately describe the experimental data. Consequently, the numerical model can be used to increase the understanding of the rotational particle behavior.

Comparing the average particle rotation frequency in Fig. S2, it is observed that for a field rotation frequency of 1.4 Hz, there is a large difference if Brownian rotation is included. In case of 2 Hz rotation, it is observed that this difference is much less and Brownian rotation may even lead to a faster average particle rotation frequency.

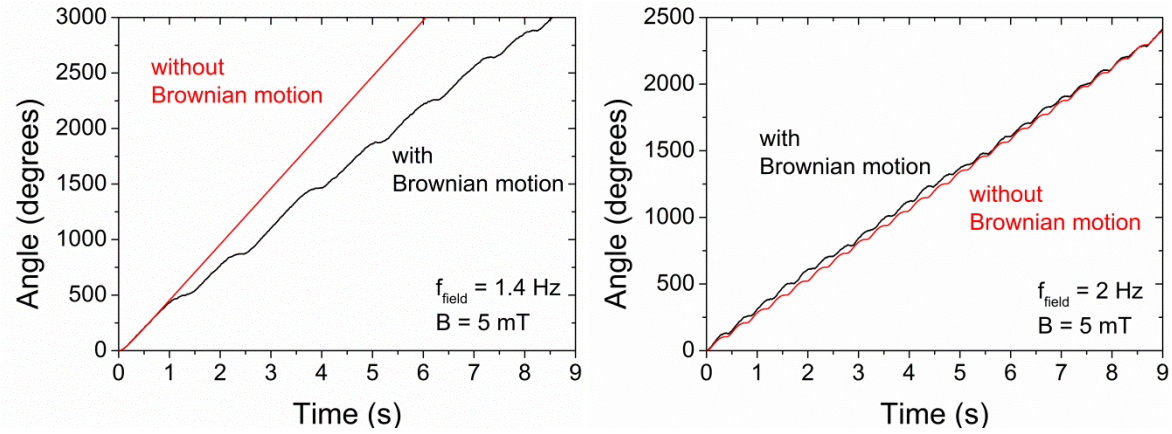

FIGURE S2 Simulated unbound particle rotation with and without Brownian motion included at a field strength of 5 mT and a field frequency of 1.4 Hz (left) and 2 Hz (right). Simulation time steps were 0.2 ms. A moment distribution is assumed consisting of 22 separate magnetic moments of equal size (i.e. 1.08 $x10^{-16}$ Am^2), which are equally distributed from -63° to +63°, in steps of 6°.

To study these differences in more detail, the average particle rotation frequency over 20 seconds of simulation was determined for different field frequencies and magnetic field strengths as shown in Fig. S3 (left). It is found that Brownian rotation most strongly influences the rotational behavior of the particles near the breakdown frequency. In particular, the breakdown frequency is lowered due to Brownian rotation. This can be explained as follows. Just below the breakdown frequency (in case of no Brownian rotation), the particle and the field are at a maximum angular difference between field and effective magnetic moment, such that no remagnetization of single magnetic moments within the particle occurs. In this configuration, a small increase in the angular difference causes the first single magnetic moments to collapse, which leads via a cascade of other collapsing moments to full remagnetization of the particle. The closer the field frequency is to the breakdown frequency, the smaller this increase needs to be for a collapse of

the magnetic moment. Brownian rotation, however, causes fluctuations on the particle orientation and can consequently trigger such a collapse even when the field frequency is below the breakdown frequency. As a result, due to Brownian rotation, the experimentally observed breakdown frequency is lower as compared to what can be expected based on the magnetic torque and hydrodynamic drag alone.

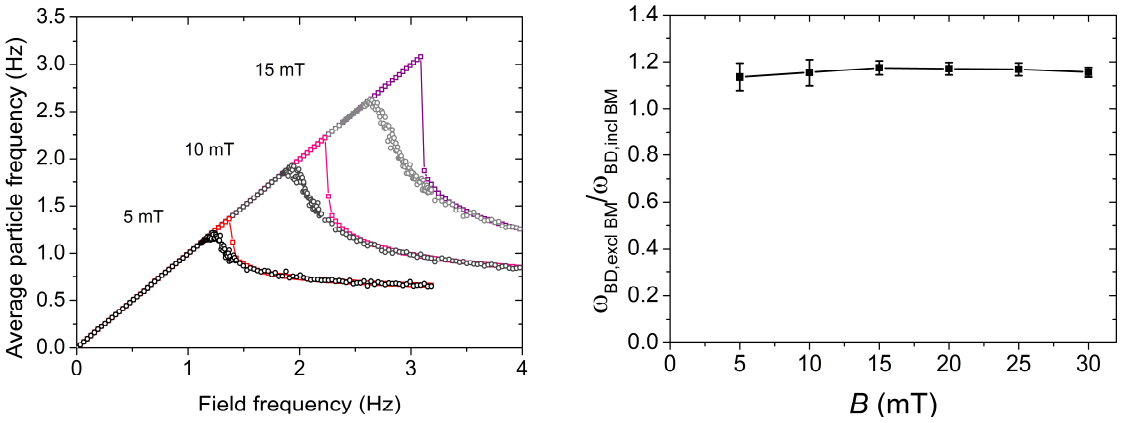

FIGURE S3 (left) Particle rotation frequency plot as a function of field frequency, for different field strengths. The open circles (black and grey-scale) correspond to simulations including Brownian rotation, whereas the open squares (red and purple) correspond to simulations without Brownian rotation. (right) Comparison between numerically obtained breakdown frequencies for the cases with and without Brownian motion. The data is shown as a function of the field strength

Furthermore, the breakdown frequency was determined for different field strengths with and without Brownian rotation. In the right panel of Fig. S3 the relative difference is shown as a function of field strength. Remarkably, it is found that the relative difference is roughly constant for the simulated field strengths. Due to the higher frequency needed to reach a collapse of a magnetic moment, the time in which Brownian fluctuations can build up, becomes less, which should result in a smaller relative difference for higher field strengths. It should be noted however, that the relative difference in breakdown frequency does not depend linearly on the relative difference in angular difference between field and particle. For example, at 5 mT, the angular difference at the breakdown frequency changes from (51±1)° to (39±5)° for respectively no Brownian rotation and with Brownian rotation included. At a field strength of 30 mT, these values are found to be (31±1)° and (26±2)°. Thus, for increasing field strengths, i.e. for an increasing breakdown frequency, the decrease in critical breakdown angle due to Brownian rotation becomes less. In spite of this, the corresponding relative decrease in breakdown frequency due to Brownian rotation is roughly constant over the range of 5 to 30 mT. Since the simulated data correspond closely to experimental results, we will use this relative difference to correct for influences of Brownian rotation on the breakdown frequency. To that end, a correction factor C_{BR} is defined which is found to be C_{BR} = 1.16±0.05 from averaging the numerically determined relative differences in Fig. S3.

S2 Magnetic torque calibration

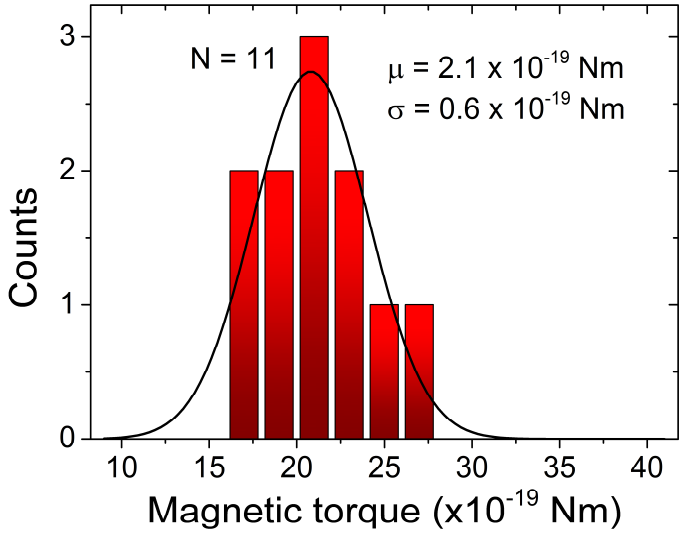

FIGURE S4 Determined magnetic torque at B = 10 mT for 11 different Dynal M-270 particles. From a Gaussian fit, a standard deviation is obtained of 28%.

S3 Dose-response curve of particle binding to adsorbed antibodies

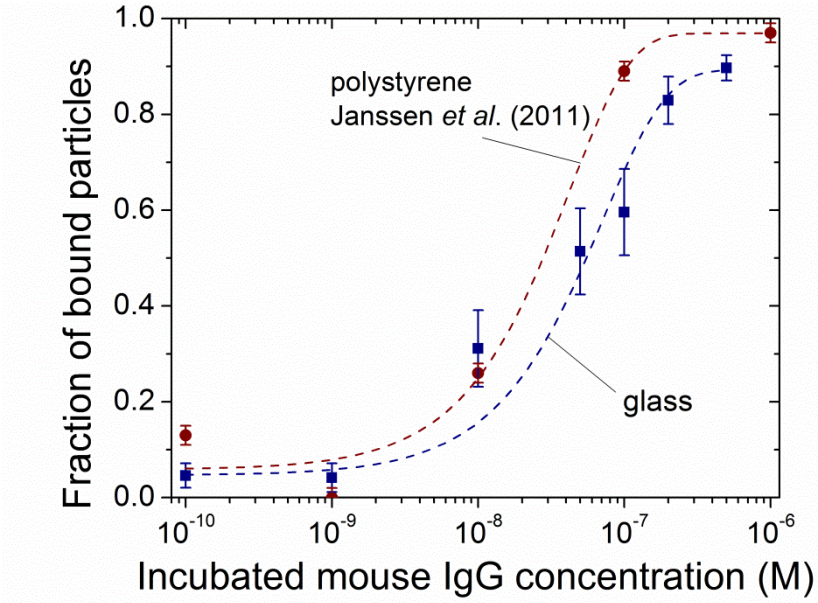

FIGURE S5 Dose-response curve of the fraction of Protein G-coated magnetic particles that bind to Mouse IgG physisorbed on a glass substrate. To compare, the dose-response curve of Janssen et al. 2011 is plotted as well, who physisorbed Mouse IgG on polystyrene. The dashed lines are guides to the eye. Data is obtained by incubating functionalized particles for 5 minutes and subsequently turning the fluid cell upside down, followed by particle counting on the functionalized surface and of the sedimented unbound particles. The binding of Protein G-coated particles to Mouse IgG is slightly less efficient on a glass substrate compared to a polystyrene surface.

S4 Estimation of the number of single bonds

From the dose-response curve in Fig. S5 it follows that the fraction of bound particles is 40 ± 5% for the used Mouse IgG incubation concentration of 50 nmol/L. A part of these bonds is due to non-specific binding, and we assume the fraction of non-specifically bound particles to be equal to what we find in control experiments: 5 ± 3% of all particles. Considering only unbound and specifically bound particles, the probability for specific binding to one or more antibodies is 37 ± 8%. This value can be used to estimate the probability of obtaining single bonds. To this end we assume random adsorption of antibodies to the substrate which we describe with Poisson statistics, i.e. the probability to obtain N bonds in a surface region D is given by

$$P(N(D)=k)=\frac{(\lambda D)^k}{k!}\exp[-\lambda D] \tag{S5}$$

In which k is an integer number and λ is the surface density of antibodies, which is actually unknown. Also unknown is the effective surface region probed by one single magnetic particle. The product λD can however be determined as we have measured the probability of at least one bond: $P(N(D) \geq 1) = 37 \pm 8\%$ and therefore $\lambda D = 0.46 \pm 0.14$. Note that from this value we can estimate the antibody surface density. Taking into account the maximum length of an antibody, 15 nm, then the interaction radius of a 2.8 μm diameter magnetic particle is approximately 200 nm, corresponding to an interaction area of 0.13 μm^2. Therefore $\lambda = 3.5 \pm 1.4$ μm^{-2}, and compared to the incubated IgG concentration, this is only a fraction of $(6 \pm 2) \times 10^{-5}$. Due to the diffusion-limited adsorption, such small adsorbed fractions might be expected. In addition, as antibody adsorption is a random process, many antibodies will be ill-oriented and do not allow for bond formation.

Since we have determined λD, we estimate the probability of single-bond formation to be $P(N(D) = 1) = 29 \pm 4\%$ and the probability of multiple bond formation to be $P(N(D) \geq 2) = 8 \pm 4\%$. Expressed as a fraction of all specific bonds, 78 ± 11% will be single bonds and 22 ± 11% multiple bonds. Therefore we conclude, that for the used antibody incubation concentration of 50 nmol/l, single bonds will be formed and only a small fraction of multiple bonds. Still, it is required to discriminate between these different types of bonds in the experiments.

S5 Characterization of bond dissociation kinetics with magnetic forces

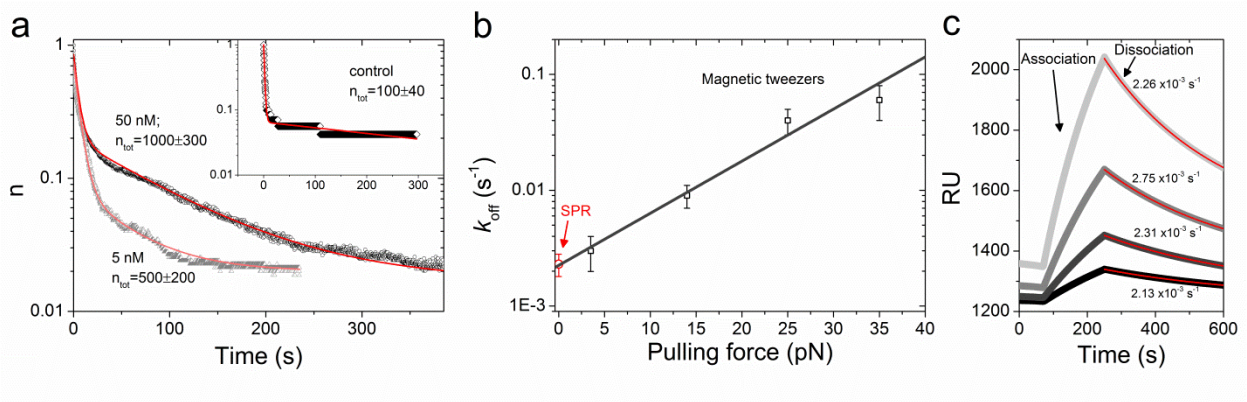

FIGURE S6 Bond characterization of the Protein G-IgG sandwich between magnetic particles and a glass substrate using a magnetic pulling force (see (19) for details about the method) after 5 minutes of incubation of the particles on the substrate. The substrate was prepared in exactly the same way as in the other experiments.

(a) Dissociation curves obtained by monitoring the number of bound particles in time after application of a magnetic pulling force of ~14 pN at $t = 0$. In the graph, the bound fraction ($n = 1$ at $t = 0$) is plotted versus time. The data is fitted (line) using a tri-exponential fit (as discussed in (19)), containing a fast dissociating fraction (weak non-specific bonds), a slowly dissociating fraction (strong non-specific bonds and multiple specific bonds), and a third intermediate fraction which corresponds to single specific bonds. The experimental data clearly shows distinct dissociation fractions, i.e. the different linear regimes on the linear-log plot, indicating that distinctly different bonds are present in the assay. The values of n_{tot} within the graph indicate the number of bound particles at $t = 0$, as found from repeated measurements (i.e. for each incubation concentration, 5 measurements were performed). The number of bound particles at t = 0 decreases with the antibody incubation concentration similar to the dose-response curve in figure S5.

(b) Determined dissociation constant (i.e. exponential decay constant) of the intermediately fast dissociating fraction of particles, as a function of applied magnetic (pulling) force. Extrapolation to zero-force yields an estimation of the dissociation constant, i.e. $(2.2 \pm 0.4) \times 10^{-3}$ s^{-1}. This value agrees with the dissociation constant of the Protein G-IgG complex measured by SPR (see panel (c)) which is indicated in the graph at a pulling force of zero pN.

From these results, it is concluded that the intermediately fast dissociating fraction corresponds to single specific Protein G-IgG bonds. From the fits it is found that this fraction, i.e. the fraction single specific bonds is 25±5%. Furthermore, 70±10% of the bound particles were found to be fast dissociating (i.e. weak non-specific bonds) and 5±3% to be slowly dissociating (i.e. strong non-specific bonds or multiple specific bonds).

(c) SPR (Surface Plasmon Resonance) data on the used Protein G-Mouse IgG couple. Different concentrations of mouse IgG were incubated on physisorbed Protein G, corresponding to the different lines. From the data corresponding to dissociation, the dissociation constant is determined by fitting the data with a single exponential, as shown by the red lines within the data. An average value is found of $(2.4\pm0.4) \times 10^{-3}$ s^{-1}, in agreement with the zero-force value derived from the force-induced dissociation data in panel (b).

S6 Remagnetization of the magnetic particles

In Fig. 4 *a*, the orientation of the magnetic field and the magnetic particle is plotted normalized to the equilibrium angle. From this plot, the orientation of the magnetic moment can be deduced. Assuming that the magnetic moment is static during actuation except when it is remagnetizing, its orientation is equal or exactly opposite to the plotted orientation of the particle (except during remagnetization, which occurs for example between t = 2.9 s and t = 3.4 s). Accordingly, the angular difference between the magnetic field and the magnetic moment at which remagnetization occurs, is found to be 35 ± 2°. This angular difference was measured for different field strengths on the same particle (Fig. S7 left) and for different particles at the same field strength of 20 mT (Fig S7 right). The decrease in angular difference for increased field strengths can be attributed to the coercive field which is overcome at smaller angles. Furthermore, a particle variation in remagnetization angle is found of roughly 10%, which indicates that the ferromagnetic properties of these particles are relatively well defined compared to the superparamagnetic properties, which are typically reported to vary strongly from particle-to-particle (8-9).

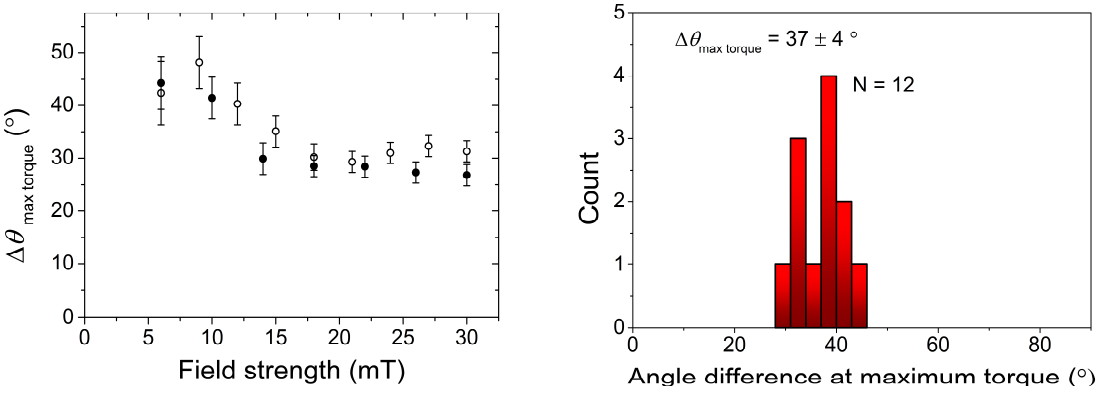

FIGURE S7 (left) Experimentally determined angular difference between field and particle upon remagnetization, shown for different field strengths. Data is obtained from two bound particles (open and closed circles represent the different particles), actuated at several field strengths. (right) Particle variation in angular difference between field and particle upon remagnetization at B = 20 mT. A variation of ~10% is obtained.

In addition, it is observed from subsequent remagnetization cycles (see Fig 4. *a* and processed data in Fig. S8) that the remagnetization angle shows only a small variation of less than 4% for a single particle. This indicates that on the timescale of our experiments, the remagnetization process is much faster and that stochastic processes in remagnetization cannot be observed.

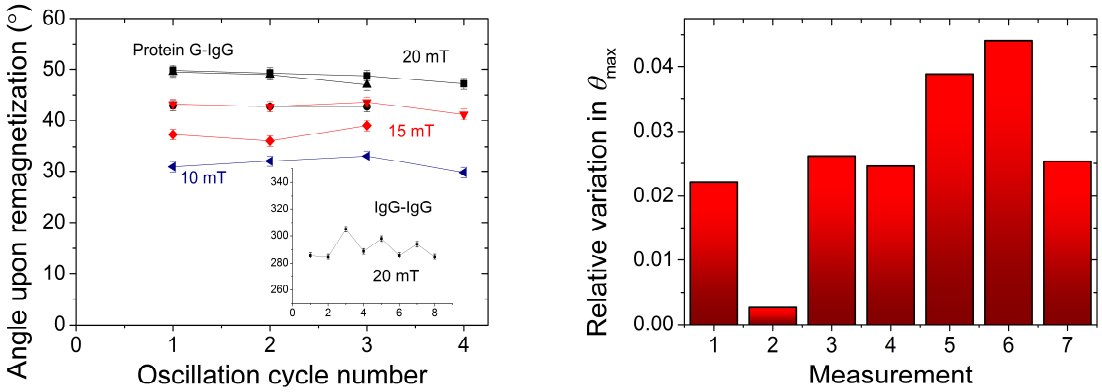

FIGURE S8 (left) Experimentally determined angular difference between field and particle upon remagnetization, shown for different situations and subsequent oscillation cycles (i.e. see Fig 4 *a*). (right) Variation in angle between field and particle upon remagnetization at subsequent oscillation cycles. Seven different measurements are shown.

We observe that within one full rotation of the magnetic field with respect to the magnetic particle, remagnetization occurs twice, indicating that remagnetization occurs over 180° degrees. Apparently, the magnetic particle exhibits an uniaxial anisotropy. Considering uniaxial anisotropy, a single ferromagnetic moment remagnetizes only when the coercive field is overcome, i.e. at an angular difference between moment and field larger than 90°. This should also be apparent in Fig. 4 *a*. Nevertheless, we observe the angular difference to be smaller than 90°, i.e. at an angle of 35 ± 2°. To reconcile this observation with uniaxial anisotropic behavior, we consider an effective particle magnetic moment.

Apparently at an angle of 35 ± 2°, a fraction of the effective particle magnetic moment already remagnetizes. For this fraction, the angular difference has to be larger than 90° (else no remagnetization is possible), and thus their orientation deviates at least 90° – 35° = 55° degrees from the effective magnetic moment of the particle. Assuming a symmetric angular distribution of the magnetic moments, the angular spread of the magnetic moments has to be at least 2 times 55°, i.e. 110°.

Fast remagnetization of the total magnetic moment can be understood using the following rationale. When a first part of magnetic moments is remagnetized over 180°, the direction of the magnetic torque due to these moments reverses, which causes the total magnetic torque on the particle to decrease. As there is no inertia, the particle immediately rotates a bit backward in order to increase the phase difference with the magnetic field such to balance the magnetic torque to the molecular torque. Consequently, due to this increase in the phase lag, more magnetic moments in the particle remagnetize, causing the particle to rotate backwards even further. This is repeated until the total moment is remagnetized. In this way, partial remagnetization speeds up remagnetization of the total magnetic moment, hence explaining the relatively fast remagnetization of the total magnetic moment.

The origin of the observed remagnetization of the particle ferromagnetic moments can be attributed to the anisotropy of the ferrimagnetic (magnetite) grains of which they consist. Three types of anisotropy are possible: magnetocrystalline, shape and surface anisotropy. It was reported by Klaue et al (2009) (18), that the saturation behavior of the ferromagnetic moment of M-280 particles corresponds quantitatively to values for the magnetocrystalline anisotropy. However, this saturation was observed at relatively large field strengths, over 100 mT, whereas for the M-270 particles, remagnetization already occurs at 5 mT. These large differences indicate a large difference between ferromagnetic properties of different types of superparamagnetic particles. Consequently, it is not unlikely, that for the M-270 particles e.g. shape anisotropy instead of magnetocrystalline anisotropy governs the ferromagnetic behavior. Moreover, based on the uniaxial remagnetization behavior observed in our experiments, it is unlikely that magnetocrystalline anisotropy of the grains is the dominant type of anisotropy, because magnetite exhibits 4 dominant easy axes. Therefore we exclude magnetocrystalline anisotropy as a possible cause for the ferromagnetic behavior of these particles.

Since the detailed shape of the magnetite grains is unknown, it is difficult to estimate the significance of surface anisotropy. Shape anisotropy however can easily allow for uniaxial anisotropy of the grains, as the presence of one elongated dimension with respect to the others would already cause this type of anisotropy. By estimating the anisotropy energy density for a magnetite prolate spheroid, we find that for a deviation larger than 5% in aspect ratio compared to a sphere, shape anisotropy dominates over magnetocrystalline anisotropy.

Note that one magnetic particle contains a large ensemble of grains with a log-normal size distribution and a random orientation. Only the large grains contribute to the remanent moment of the particle. The net remanent moment can be due to the discrete character of a limited number these grains or to a production process that does not yield a completely random distribution.

S7 Frequency-dependence of Protein G–IgG twisting

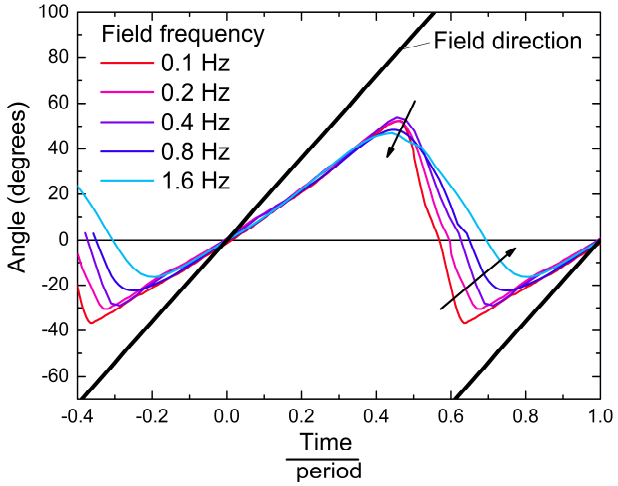

FIGURE S9 Twisting behavior of the Protein G–IgG complex is plotted for different frequencies of the rotating magnetic field at 20 mT. Note that time on the x-axis is transformed such that the curves can be directly compared, i.e. the time is divided by the period of the oscillatory behavior. Clearly, the behavior at different field frequencies is nearly the same in case the magnetic moment is not remagnetizing. This is another indication that hydrodynamic drag has a negligible effect on the oscillatory behavior. For increased field frequencies the maximum angular excursion shows a slight decrease, and more pronounced differences are observed in the remagnetizing behavior.

S8 Variation in measured torsion constant

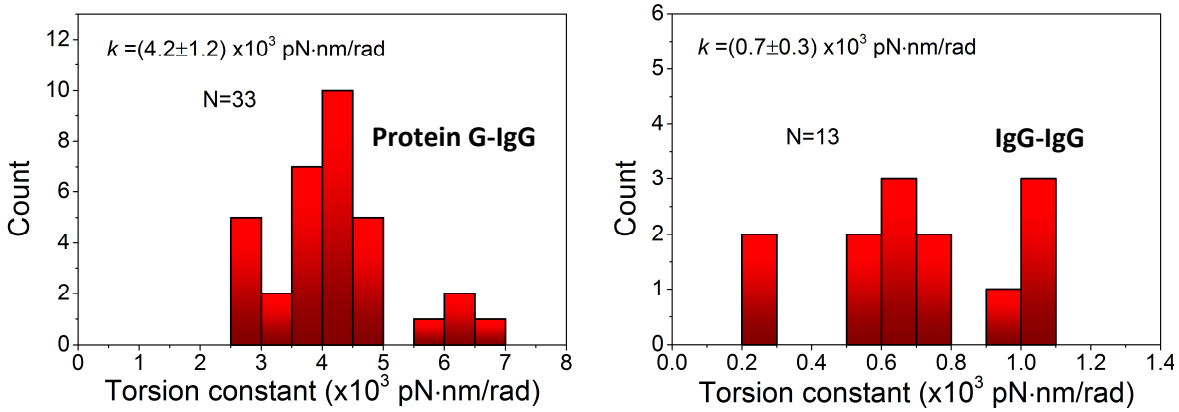

FIGURE S10 Histograms of the measured torsion constants on individual particles for (left) the Protein G-IgG complex and (right) the IgG-IgG complex. A standard deviation is determined of respectively ~30% and ~40%.

S9 Angular fluctuations of bound particles in the absence of a magnetic field

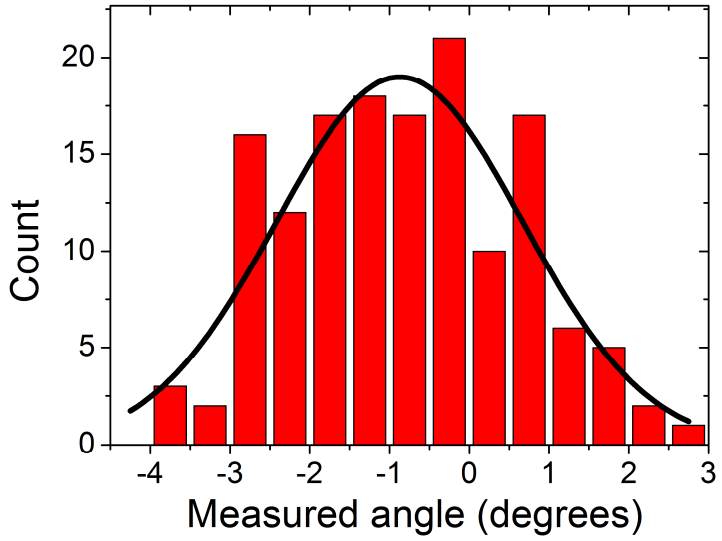

FIGURE S11 Histogram of angular fluctuations corresponding to data of the particle shown in Fig. 4 *a* in case no external field is present. Assuming that these fluctuations are caused by thermal energy, it is possible to determine the torsional spring constant without magnetic actuation of the magnetic particle. Balancing thermal energy and potential energy for a harmonic spring (with spring constant k), on average, the root-mean-squared angular orientation will be:

$$\theta_{rms}^2 = \frac{1}{N}\sum_{i=1}^{N}\left(\theta_i - \bar{\theta}\right)^2 = \frac{k_B T}{k} \qquad \text{(S6)}$$

with N the number of measurements and $\bar{\theta}$ the average angle. First, θ_{rms} is determined from the observed oscillations (measured at room temperature T = 293 K) by fitting the distribution with a Gaussian distribution. Then, using Eq. S6 a torsional spring constant is obtained of $k = (5.5\pm0.8) \times 10^3$ pN·nm/rad. It should be noted however, that the measured excursions are close to the estimated error due to the angular tracking from the images, i.e. ~2 degrees. In addition, as the sample is still located in the center of the magnetic setup, a minor remanent magnetic field is still present of 0.1 mT up to 1 mT. This may affect the angular fluctuations and thus the angle distribution.